Dynamics of two-dimensional flow around a circular cylinder with flexible filaments attached

Jian Deng
Department of Mechanics, Zhejiang University, Hangzhou 310027, People's Republic of China

Xuerui Mao*
Faculty of Engineering, University of Nottingham, University Park, Nottingham NG7 2RD, United Kingdom

Fangfang Xie
School of Aeronautics and Astronautics, Zhejiang University, Hangzhou 310027, People's Republic of China

(Received 10 January 2019; published 25 November 2019)

A direction adaptive approach for the reduction of drag and the suppression of lift fluctuation in flow passing a circular cylinder is developed. Flexible filaments are attached to the surface of the cylinder, and different configurations, including the number, lengths, and angles of attachment of the filaments, as well as their tension and bending features, are investigated. In this comprehensive numerical study, the configuration with two filaments 180° apart is found to be optimal for drag reduction and lift fluctuation suppression and is adaptive to the direction of the incoming flow. A drag reduction of 10.8% and a lift fluctuation suppression of 34.6% can be achieved as one filament is attached to the rear stagnation point and the other to the front stagnation point. The hairy coating resembled by 12 evenly attached filaments is also considered. Though marked drag reduction has not been found for this configuration, we leave it an open question for future studies to explore various properties of the filaments in turbulent flow, whose interaction with the filaments would be significant.

DOI: 10.1103/PhysRevE.100.053107

I. INTRODUCTION

A long cylinder placed in cross-flow is subject to vibrations caused by periodic hydrodynamic forces, accompanied by a famous phenomenon known as Kármán vortex streets, leading to vortex-induced vibration (VIV) of the cylinder [1]. The VIV and its mitigation widely exist in practical engineering, such as bridges, high-rise buildings, heat exchangers, and ocean structures. A typical example is the deep-water risers which are commonly used to connect the sea bed to offshore drilling platforms. As the depth reaches 1000–2000 m, VIV becomes one of the main challenges for safe and cost-effective production of oil and gas [2].

VIVs can be suppressed in both passive and active manners, and the latter can be further classified into active open-loop (for the cases with actuators and without sensors) and active closed-loop (with actuators and sensors), as reviewed in [3]. Most active controls use various forcing devices, such as rotary [4–6], streamwise [7,8], and transverse oscillations [9,10] of a bluff body, inflow oscillation [11], electromagnetic forcing [12], blowing or suction [13,14], distributed forcing [15], etc. Constantly active methods require energy inputs and therefore need more complicated mechanical devices, particularly for those with closed-loop controls, where the feedback control algorithms have to be carefully designed to minimize the portion of energy input. Accordingly, the active methods are less desirable in practice, while passive methods referring to those that do not consume energy have predominance in terms of their easy implementation.

Passive control can be achieved in two approaches: either by modifying the shape of the body or by adding auxiliary devices. For instance, it was found that a dimpled circular cylinder had a lower drag coefficient than a smooth cylinder from Reynolds number 4×10^4 to 3×10^5 [16]. A spanwise waviness was introduced to the front stagnation face of a rectangular cylinder, which led to the suppression of vortex shedding due to the spanwise waviness [17]. This concept was extended to a circular cylinder by changing the straight axis of the cylinder into a sinusoidal axis along the spanwise direction and by spirally attaching hemispherical bumps on the cylinder surface, producing an effect similar to that observed for the flow over a rectangular cylinder [18]. Various auxiliary devices, such as an additive smaller cylinder or control rod [19], hydrofoils [20], helical strakes [21], as well as fairings [22], have proved to be effective for VIV suppression. Another widely used device is the splitter plate, which is favored due to its simple geometry. Since the first attempt by [23], a series of experimental and numerical works have been performed [24–27], and drag reduction and vortex shedding suppression were achieved under specific conditions. Studies have also been performed on a splitter plate hinged to, and allowed to rotate around, the rear point of a cylinder [28,29]. It was found that both the vibration and force fluctuations of the cylinder can be significantly suppressed [30].

In addition to rigid splitter plates, recently, flexible plates or filaments have received significant attention for their role in passive flow control [31], as they can self-adapt to

*Corresponding author: xuerui.mao@nottingham.ac.uk

various flow directions without any active input of energy [32]. This was inspired by animal locomotion where the flapping filaments have a critical role on extracting energy from the ambient flow [33–35]. In a numerical study on flow around a circular cylinder partially coated with hair, represented by a set of articulated rods, the reductions of the average drag of up to 15% and lift fluctuation up to 40% were achieved [31]. It was reported that an elastic filament attached to the rear of a circular cylinder could both produce a net lift force and reduce the mean drag force on the cylinder by breaking the spontaneous symmetry [36]. In the simulation of the vortex-shedding-induced vibration of a flexible splitter plate behind a cylinder, it was found that the flexibility of a plate adversely modulates the drag and lift forces acting on the cylinder [37]. Further, the fluctuation of lift forces and VIVs on a circular cylinder were found to be suppressed efficiently by using an attached flexible filament. This is because energy in the wake of the cylinder went into driving the oscillations of the filament rather than forming vortices, and consequently, the filament motion pushed vortices away and stabilized the flow [38]. More recently, a laminar flow (Re = 100–300) over a circular cylinder with two attached flexible filaments was investigated [39]. The cylinder was fixed, and the filaments with the same properties were symmetrically arranged along the rear surface of the cylinder. They found that the mean drag and the lift fluctuation can be reduced effectively, with the lowest values achieved at an optimal separation angle of 90° between the two filaments.

From the above literature review, the strategy of using multiple filaments to enhance the control effect has been explored. However, in all these efforts, the filaments were attached at the rear of the bluff body to control the flow wake [31,39]. This is based on a prerequisite that the direction of incoming flow is known and fixed. In real applications, as the orientation of the riser or the direction of the ocean currents varies, the fixed ends of the filaments will deviate from their ideal attaching positions. The control effects of the filaments at varying incoming flow conditions have not been clarified in the literature. In the case that the incoming flow direction has a critical impact on the filaments, multiple filaments attached around the outer surface of the bluff body should be considered, to adapt to the incoming flow and ensure the presence of filaments in the wake region. In this work, we investigate the flow around a circular cylinder attached with multiple flexible filaments, aiming to find a configuration insensitive to the change of the flow direction.

The immersed boundary method (IBM) has been employed in most existing simulations of the interaction of filaments and fluid flow. This method was first developed to model the moving boundaries in heart-valve simulations [40]. It is efficient since all the simulations can be carried out with the fixed Cartesian grid and only a virtual force term is required in the momentum equation. Under the original derivation of Peskin's IBM, it was assumed that the fluid and the structure are with the same material, or in other words, the immersed boundary or structure does not add any mass beyond what would be there anyway if the boundary or structure was replaced by fluid. A direct method used to handle boundary mass was to spread that mass out onto the fluid grid, causing a density variation in the Navier-Stokes equations, which complicates the numerical solver of those equations [41]. To handle this problem, various numerical methods based on the immersed boundary framework have been proposed [42–44], most of which were originated from Zhu's treatment [41] by splitting the elastic filament into massless and massive components. These methods differ in the way to distribute the elastic force and the reacting force between the massless and massive components of the filament. A representative implementation is the penalty IBM, which has been extensively applied to various problems: 2D and 3D parachutes [45,46], flexible clap and tiny insect flight [47], dry foam dynamics [47], and inextensible vesicles [48]. This method has been proved to be practical and effective when considering a deformable body with mass.

Another optional treatment of the immersed boundary was proposed by [49], which in our understanding is a variation of the feedback forcing scheme developed specifically for rigid immersed boundaries [50]. In this new treatment, the fluid is governed by the Navier-Stokes equations and the filament by its own set of equations. While differing from the traditional Peskin's method, they are solved independently and the interaction between the two equations is applied as a momentum forcing term to each. The inextensibility condition is satisfied in the equations of motion for the filament by first calculating the tension force at the intermediate time step that is required to prevent any extension, and the errors introduced at previous time steps are penalized. They also introduced a method for handling collisions between adjacent filaments by using an artificial repulsive force to account for the interaction of two close filaments through the Dirac δ function [49]. In our study, we follow the IBM considering the inertial effect proposed by [41] and the treatment of avoiding collision proposed by [49].

The remainder of this paper is organized as follows: In Sec. II we present the formulation of the problem and describe the simulation methodology for the filaments in a fluid flow. Then the results will be presented in three parts in Sec. III. In Sec. III A we study a single filament attached to the circular cylinder at the downstream stagnation point, focusing on the control effects at various attaching positions. Then, in Sec. III B we attach two filaments 180° apart and examine the direction adaptivity of this configuration. Furthermore, in Sec. III C we study a dense distribution of filaments along the cylinder surface, with 12 filaments considered, to evaluate the drag reduction by "hairy coating." Finally, in Sec. IV we draw our conclusions.

II. PROBLEM DEFINITION AND NUMERICAL METHOD

A. Problem definition

We consider the two-dimensional flow around a fixed circular cylinder attached with various numbers of filaments. For a single filament, its attaching point is denoted by the angle θ, measured from the downstream stagnation point of the cylinder, as shown in Fig. 1. For multiple filaments, their distributions will be defined based on the most downstream filament, as will be discussed later in Sec. III. For all simulations, we fix the Reynolds number at $\mathrm{Re} = U_\infty D/\nu = 100$, where D is the diameter of the circular cylinder, U_∞ is the streamwise velocity far upstream, and ν is the kinematic viscosity. All the

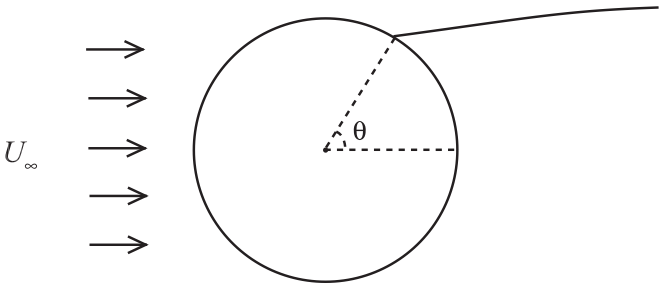

FIG. 1. Definition of the attaching angle θ of a filament.

forces will be nondimensionalized by $\frac{1}{2}\rho U_\infty^2 D$, where ρ is the fluid density, to obtain their respective coefficients.

B. Numerical methods

We use the open source code OPENFOAM to solve the time-dependent, incompressible form of the Navier-Stokes equations [51]. The differential form of the momentum equation is shown in Eq. (1), where an extra forcing term $\mathbf{f}$ is included to represent the objects immersed in the fluid flow. The forcing term $\mathbf{f}$ is calculated by IBM [40]. We adopt a Penalty IBM (PIBM) to take into account the gravity and inertial effects of filaments. Note that we actually consider neutrally buoyant filaments in the current study to avoid the direction preference when there are multiple filaments. The penalty part of the algorithm is kept in the following presentation only to take into account the inertial effects of the filaments, of which the detailed implementations can be found in our previous study [52].

Equation (1) are the Navier-Stokes equations for viscous incompressible fluid. $\rho, \mathbf{u}, p$ are the density, velocity, and pressure of the fluid, respectively:

$$\rho\left(\frac{\partial \mathbf{u}}{\partial t} + \mathbf{u}\cdot\nabla\mathbf{u}\right) = -\nabla p + \mu\nabla^2\mathbf{u} + \mathbf{f},$$
$$\nabla\cdot\mathbf{u} = 0. \tag{1}$$

The extra forcing $\mathbf{f}$ in Eq. (1) is calculated by the integration of the Lagrangian forcing density $\mathbf{F}(s,t)$ on the filaments weighted by a Dirac δ function,

$$\mathbf{f}(\mathbf{x},t) = \int \mathbf{F}(s,t)\delta(\mathbf{x}-\mathbf{X}(s,t))ds, \tag{2}$$

where $\mathbf{x}$ is the spatial coordinate of the domain, and $\mathbf{X}$ represents the Lagrangian points which are linked by one-dimensional rods to model the thin filament.

The force $\mathbf{F}(s,t)$ consists of three parts:

$$\mathbf{F} = \mathbf{F}_E + \mathbf{F}_K + \mathbf{F}_C, \tag{3}$$

where $\mathbf{F}_E$ is the elastic force induced by the deformation of the filaments, $\mathbf{F}_K$ is the restoring force considering the mass of the filaments, and $\mathbf{F}_C$ is the repulsive force to avoid collision between different filaments, or between the filaments and the cylinder.

$\mathbf{F}_E$ can be computed from

$$\mathbf{F}_E = -\frac{\partial E}{\partial \mathbf{X}}, \tag{4}$$

where E is an energy function. Here we impose two elasticities on these rods, one resisting stretching and compression, and the other resisting bending. The energy function $E[\mathbf{X}(.)]$ in Eq. (4) can therefore be formalized as

$$E[\mathbf{X}(\cdot)] = \frac{1}{2}k_s\int\left(\left|\frac{\partial X}{\partial s}\right| - 1\right)^2 ds + \frac{1}{2}k_b\int\left|\frac{\partial^2 X}{\partial^2 s}\right|^2 ds, \tag{5}$$

where k_s and k_b denote the coefficients for stretching and bending, respectively. We note that variables defined on the filament domain are spread to the fluid domain using the Dirac δ function, which has been widely used in IBM. Its discrete form is expressed as

$$\delta_h(\mathbf{X}) = h^{-2}\phi\left(\frac{X}{h}\right)\phi\left(\frac{Y}{h}\right), \tag{6}$$

where X and Y are the streamwise and vertical components of $\mathbf{X}$, h is the length of the computational cell, and ϕ is a function defined as [53]

$$\phi(r) = \begin{cases} \frac{3-2|r|+\sqrt{1+4|r|-4r^2}}{8} & \text{if } |r| \leqslant 1; \\ \frac{5-2|r|-\sqrt{-7+12|r|-4r^2}}{8} & \text{if } 1 < |r| < 2; \\ 0 & \text{if } |r| \geqslant 2. \end{cases} \tag{7}$$

To take into account the gravity or inertial effect of the filaments, we split the immersed boundary conceptually into two Lagrangian components connected by a spring. The *massless* component $\mathbf{X}(s,t)$ on one end of the spring interacts with the fluid exactly as that in a traditional IBM implementation, i.e., it moves as the local fluid velocity and the induced solid stress is distributed to the surrounding fluid cells. The *massive* component $\mathbf{Y}(s,t)$ is connected to the massless component by the stiff spring and acts on the massless component through the restoring force $-\mathbf{F}_K$ [Eqs. (8) and (9)]. We note that the massive component does not interact with the fluid directly. According to Newton's law of motion, the massive component and the immersed boundary move independently, only with the forces generated by the stiff spring. If the gravity is included, it is imposed on the massive component of the immersed boundary. Since the spring is usually very stiff, the massless and massive components stay very close to each other, and therefore the whole system acts like an immersed boundary with mass:

$$\mathbf{F}_K(s,t) = K[\mathbf{Y}(s,t) - \mathbf{X}(s,t)], \tag{8}$$

$$\rho_s(s)\frac{\partial^2\mathbf{Y}}{\partial^2 t} = -\mathbf{F}_K(s,t) - \rho_s(s)\mathrm{Fr}\frac{\mathbf{g}}{g}, \tag{9}$$

where $\mathrm{F_r} = gL/U_\infty^2$ is the Froude number.

The repulsive force between one filament with another or the cylinder is given by

$$\mathbf{F}_C(s,t) = \int \delta(\mathbf{X}(s,t) - \mathbf{X}'(s',t))\frac{\mathbf{X}-\mathbf{X}'}{|\mathbf{X}-\mathbf{X}'|}ds', \tag{10}$$

where $\mathbf{X}'(s',t)$ is the Lagrangian point of another filament or the circular cylinder.

The choice of K depends on spatial and temporal resolution, in order to preserve the numerical stability. Sufficiently large values of K and k_s were suggested by previous studies

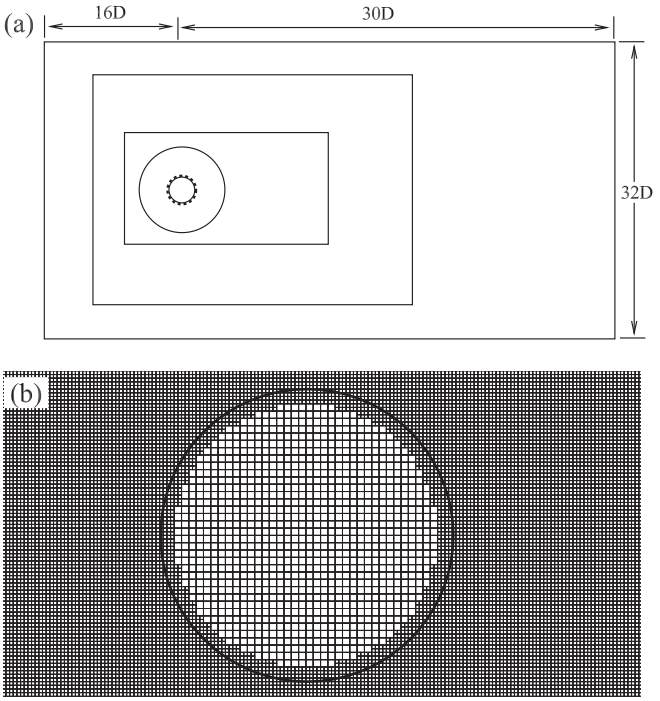

FIG. 2. Schematics of the (a) computational domain, in which the rectangular and circle zones are mesh refined, and (b) mesh distributions around the circular cylinder.

[41,53]. Here, $K = 100,000$ and $k_s = 200,000$ are adopted to meet the in-extensibility condition of the filament [52].

The no-slip boundary conditions on the filaments are applied by matching the velocity of the filament and the fluid flow around it at each Lagrangian point on the filament:

$$\frac{\partial \mathbf{X}}{\partial t}(s,t) = \mathbf{U}(s,t) = \int \mathbf{u}(\mathbf{x},t)\delta(\mathbf{x} - \mathbf{X}(s,t))d\mathbf{x}. \quad (11)$$

C. Numerical validation

The computational domain is shown in Fig. 2(a), in which three levels of mesh refinements are implemented, leading to the finest mesh around the circular cylinder. The origin point of the coordinate system is fixed at the center of the cylinder. The inflow, outflow, and far-field boundaries are 16D, 30D, and 16D away from the center, respectively. To assure time-discretization independence, a relative small time step size $dt = 0.0005$ is used for all cases, indicating that about 10 000 time steps per cycle have been considered.

To validate our spatial resolution, we carry out self-consistency tests to assure satisfactory independence of the force calculations with respect to the mesh discretization. Different mesh sizes, with the lengths around the cylinder, from $H = 0.05D$ (a coarse mesh with 19 212 cells and 20 cells along the cylinder diameter) to $H = 0.006\,25D$ (a fine mesh with 1 188 922 cells and 160 cells along the cylinder diameter) are used. As shown in Fig. 3, for the flow around a circular cylinder at the Reynolds number adopted in this work, Re = 100, the results show that our medium-mesh resolution ($H = 0.0125D$) provides satisfactory accuracy. Therefore, we use the medium mesh of $H = 0.0125D$ for all the following calculations.

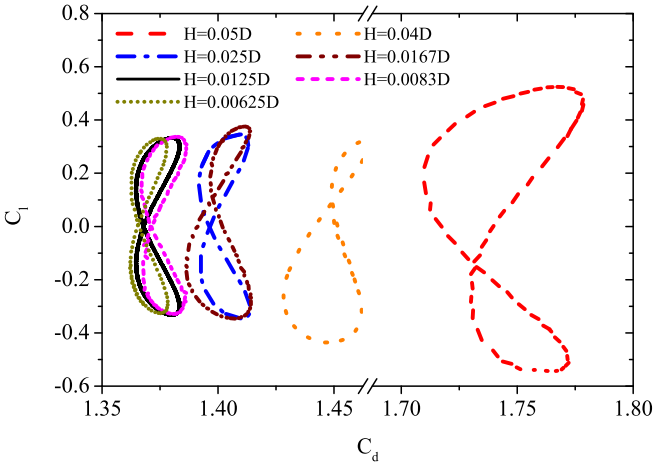

FIG. 3. Phase diagram of the drag and lift coefficients for flow around a circular cylinder for different mesh sizes, in the range $H = 0.05D$–$0.00625D$.

For the flow around a clean circular cylinder at Re = 100, we show the force history and wake flow in Fig. 4. We find that a good agreement is obtained in comparison with the previous simulations. The average drag coefficient $\langle C_d \rangle$ is 1.374, very close to the result of [54], where a value of 1.379 was found. The peak-to-peak amplitude of the lift coefficient was $\Delta C_l = 0.668$, according well with the previous numerical result of 0.62 [54]. Fourier analysis of the fluctuating lift yields a Strouhal number $\mathrm{St} = f_v D/U = 0.164$, in which f_v is the dominant frequency, consistent with the previous numerical result of 0.167 [54]. Our results are also within the ranges of the previously reported values. For example, the average drag

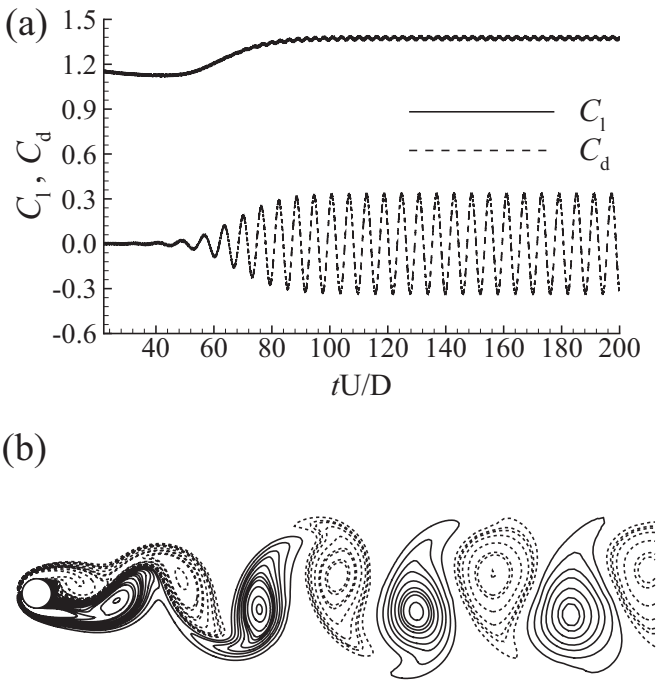

FIG. 4. (a) Time histories of lift and drag coefficients and (b) vortical contours (solid lines for positive values and dashed lines for negative values) for the flow around a circular cylinder at Re = 100.

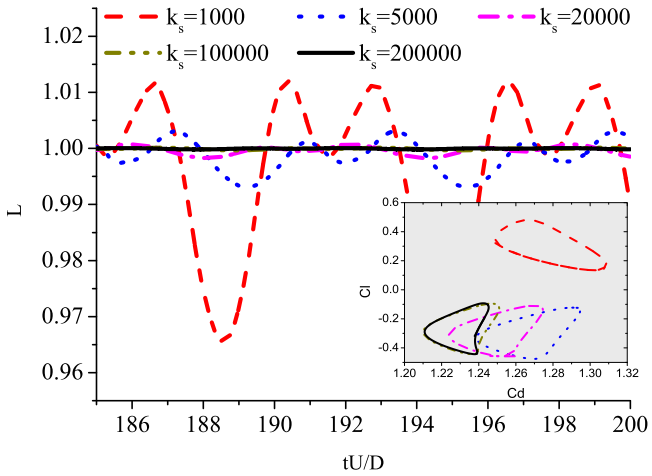

FIG. 5. Time histories of the filament lengths for the flow around a cylinder with a single filament attached to its downstream stagnation point, with different values of k_s considered. The inset shows their corresponding phase diagrams of the drag and lift coefficients.

coefficient, the lift amplitude, and the Strouhal number were $\langle C_d \rangle = 1.39$, $\Delta C_l = 0.64$, and $St = 0.167$, respectively, in Ref. [38]. The average drag coefficient and the lift amplitude were $\langle C_d \rangle = 1.33$ and $\Delta C_l = 0.664$, respectively, in Ref. [55].

We note that the number of Lagrangian points on the circular cylinder varies accordingly in the range of 63–502 for different spatial resolutions. The filaments are segmented to the same length scale with their surrounding Eulerian mesh size, for example, for a filament of $1D$ length, 80 Lagrangian points are used for the mesh resolution $H = 0.0125D$. According to our previous study [52], such a strategy of choosing the Lagrangian point spacings close to their surrounding Eulerian mesh size is appropriate to the simulations of flow around a flexible filament.

It should be pointed out that the hydrodynamic forces are calculated by integrating Eq. (3) along the Lagrangian points on the circle (here only the term $\boldsymbol{F}_K$ is relevant). When considering attached filaments, the same integration is performed on the filaments to obtain the hydrodynamic forces on each filament. If not specifically noted, the drag and lift forces discussed in the following include both contributions from the circular cylinder and the filaments. It is possible to study the hydrodynamic forces on the individual filament, but as we introduce numerically the repulsive force F_C in Eq. (3) to avoid the collisions between different filaments, it may impose nonphysical extra forces on the filaments. Since these repulsive forces are internal forces, they will be canceled as we consider the hydrodynamic forces on the cylinder-filaments system in total.

As we discussed in the last section, sufficiently large values of K and k_s should be adopted. Here, we carry out independent tests of k_s on the flow around a cylinder with a single filament attached to its downstream stagnation point, with $L = 1.0D$, $\rho_s/\rho_f = 0.1$, and $k_b = 0.005$. Five different values of k_s are tested, as shown in Fig. 5. Apparently, when k_s is small, the filament length fluctuates with time and the inextensibility condition cannot be satisfied. As k_s increases to 200 000, the filament length stays constant at $L = 1.0D$ with time. Indeed, the forces vary little from $k_s = 100\,000$ to 200 000, showing satisfactory converged results.

III. RESULTS AND DISCUSSION

A. Attached with a single filament

It has been reported that the drag force on a circular cylinder immersed in a uniform flow can be reduced by attaching a flexible filament to its downstream stagnation point, and the lift fluctuation can be suppressed simultaneously [36,38]. It was also found that several properties of the filament, including the length, density, and rigidity, have nontrivial impacts on the flow field and subsequently the hydrodynamic forces on the cylinder. Based on these parameters, the natural angular frequency of the filament can be defined by [38]

$$\omega_n = (1/L)^2 \sqrt{k_b/\rho_s}. \tag{12}$$

We can then define a nondimensional frequency by

$$\omega_r = 2\pi f_v/\omega_n, \tag{13}$$

which denotes the ratio between the vortex shedding frequency in a clean cylinder flow and the natural frequency of the filament.

We present the phase diagram of drag and lift coefficients on a cylinder attached with a filament in Fig. 6. The data is collected after running the simulation for a sufficiently long time interval. Two lengths, $L/D = 0.5$ and $L/D = 1.0$, are considered. The attachment point is varied from $\theta = 0^o$ to 180^o, while $\theta = 180^o$ to 360^o is not considered due to the symmetry of the problem. The forces on a clean cylinder are also included in Fig. 6 for comparison (denoted by $*$).

It is evident that the attaching point of the filament has a significant effect on the forces as shown in Fig. 6. With the attachment near the downstream stagnation point (0^o), the drag force is reduced and the lift force fluctuation has a lower amplitude compared to the clean cylinder case. Specifically, at $L = 1.0D$ and $\omega_r = 7.28$, the average drag coefficient is reduced 13% and the lift fluctuation 48%. At $L = 0.5D$ and $\omega_r = 1.15$, the reductions of drag and lift fluctuation are 9.8% and 30.8%, respectively. It is clear that the control effect maximizes at $\theta = 0^o$. Conversely, with a filament attached to the upstream stagnation point (180^o), both the average drag force and the fluctuation of lift increase at $L = 1.0D$, as shown in Fig. 6(b). However, it is interesting to find that when the filament is short, i.e., $L = 0.5D$, the phase diagram of the forces for the $\theta = 180^o$ case is very close to that of the clean cylinder, as shown in Fig. 6(b).

We also note that both the 0^o and 180^o cases experience nonzero net lifts, ignoring the fact that the geometrical configurations are symmetric with respect to the incoming flow direction. Both positive [0^o in Fig. 6(a)] and negative [0^o in Fig. 6(b)] net lifts can be observed. This symmetry breaking behavior has been observed and discussed in previous studies [36], which suggests that the side preference for the lift deflection depends on the initial conditions and the numerical errors brought by either the mesh or the numerical schemes.

Examining various attaching angles of the filament shown in Fig. 6, we find that in the range $\theta = [0^o, 40^o]$, the average drag is reduced, while the lift fluctuation does not change

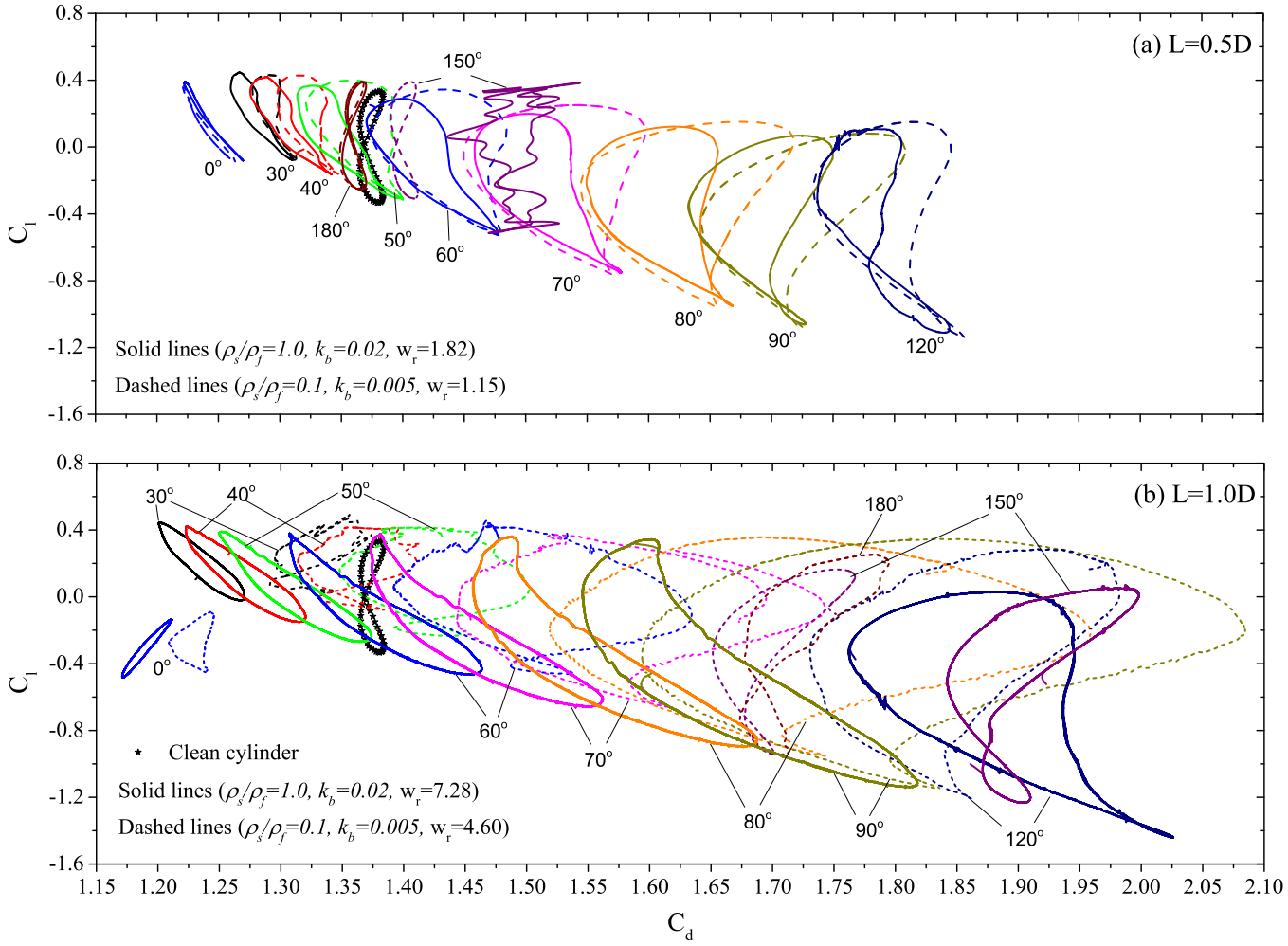

FIG. 6. Phase diagram of the drag and lift coefficients for flow around a circular cylinder attached with a single filament at various attaching points marked by different colors. The filament lengths are (a) $L = 0.5D$ and (b) $L = 1.0D$.

significantly. We note that $\theta = 50^o$ is a critical value at which the drag is reduced at $\omega_r = 7.28$ while being increased at $\omega_r = 4.6$ for $L = 1.0D$, as shown in Fig. 6(b). As a coincidence, this critical angle of 50^o is very close to the angle of separation point, which is just above 60° for the clean cylinder [56]. As we further increase the angle of attachment, the drag increases, reaching its maximum at 120^o for both lengths and frequency ratios.

When the simulation converges, the filament motion is modulated to a periodic flapping with the period very close to that of the vortex shedding behind the clean cylinder. In Fig. 7, we plot the filament positions at subsequent time intervals in one flapping cycle. When the filament is attached to the downstream stagnation point ($\theta = 0^o$), after converging to a periodic state, its equilibrium position deviates from the center line $y = 0$, presenting an asymmetric motion [36], as shown in Figs. 7(a) and 7(c). At $L = 0.5D$, the flapping magnitude is trivial [see Fig. 7(a)], while at $L = 1.0D$, the filament tip sweeps a distance about 30% of the filament length [see Fig. 7(c)]. Ideally, the symmetry of the initial configuration with respect to $y = 0$ means that one side should not be favored over the other. However, slight numerical errors due to round-up in the simulation cause the filament to initially move in one direction before settling in this position in the wake [36]. The fluid then applies insufficient forces to the filament to cross the symmetry line $y = 0$ and thus the magnitude of flapping motion is restricted. The slightly larger drag reduction for $L = 1.0D$ compared to $L = 0.5D$ [by comparing Figs. 6(a) and 6(b) for $\theta = 0^o$] can be actually explained in the same way as a rigid splitter plate which can split near-wake vortices and suppress the wake shedding [57].

When the filament is attached to the upstream stagnation point ($\theta = 180^o$), the filament tends to attach to the surface of the cylinder at $L = 0.5D$, as shown in Fig. 7(b), leading to a very similar phase diagram of forces compared to the clean cylinder case. This behavior for short filaments is valuable, as it demonstrates a control effect adaptive to the change of flow directions in real conditions. The drag does not increase at this configuration, while when the flow reverses, the drag will be reduced. As a typical example, the tidal currents reverse once or twice a day. However, at $L = 1.0D$, as shown in Fig. 7(d), the filament is too long to be stuck to the cylinder surface, resulting in 25% increase of the average drag from the clean

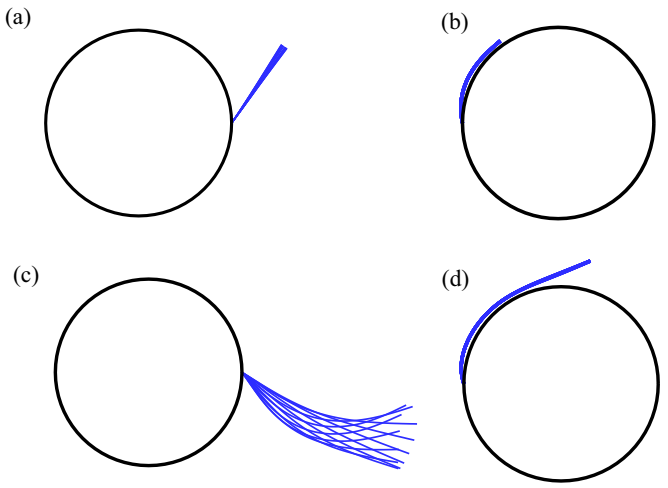

FIG. 7. Ranges of motion for a filament attached to the cylinder (a) $\theta = 0^o$ and (b) $\theta = 180^o$ for $L = 0.5D$ and $\omega_r = 1.15$; (c) $\theta = 0^o$ and (d) $\theta = 180^o$ for $L = 1.0D$ and $\omega_r = 4.60$.

cylinder case, as the filament increases the cross-area of the bluff body [see Fig. 6(b)].

B. Attached with two filaments 180° apart

As we have discussed in the last section, the advantage of using a short filament lies in the fact that it is adaptive to the change of flow directions. Here, enlightened by the results in Fig. 6, we consider two identical short filaments 180° apart, with $L = 0.5D$ and $\omega_r = 1.15$, to examine the drag reduction effect at changing flow directions. The angle of attachment θ is defined based on the downstream filament. Following this definition, the $\theta = 0^o$ case is identical to $\theta = 180^o$. It is clearly shown in Fig. 8 that the drags are reduced as the angles are small. In specific, $\langle C_d \rangle = 1.226$ and $\Delta C_l = 0.437$

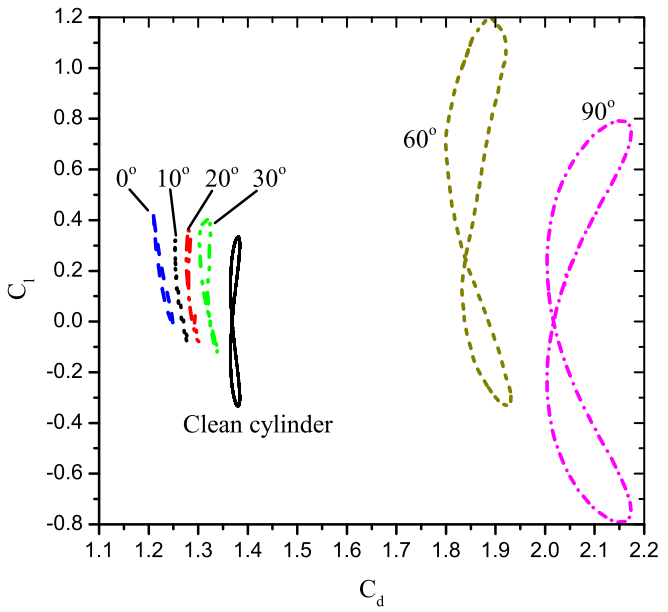

FIG. 8. Phase diagram of the drag and lift coefficients for flow around a circular cylinder with two filaments attached 180° apart.

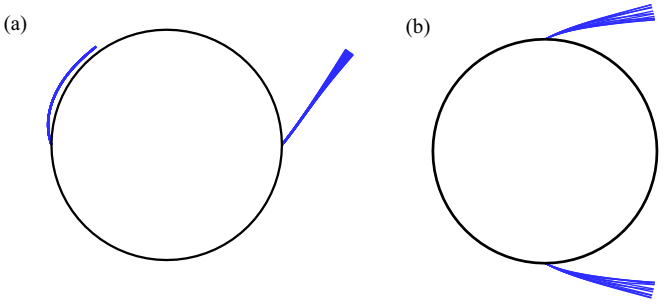

FIG. 9. Ranges of motion for two filaments 180° apart with angles (a) 0° and (b) 90°, for $L = 0.5D$ and $\omega_r = 1.15$.

at $\theta = 0^o$. The drag coefficient experiences a 10.8% reduction from the clean cylinder case, which is close to the superposition effect of attaching two filaments to the upstream and downstream stagnation points separately. Moreover, we notice that both the drag reduction and lift fluctuation suppression can be achieved within a range of small angles $\theta = 0^o - 30^o$. Therefore, we conjecture that attaching two filaments 180° apart can produce appreciated drag reduction and lift fluctuation suppression effects, and this control effect is direction adaptive.

In Fig. 9, we show the ranges of motion for $\theta = 0^o$ and $\theta = 90^o$. The recorded trajectories for the two filaments at 0° are the exact superposition of Figs. 7(a) and 7(b) for the single filament. For $\theta = 90^o$, as seen in Fig. 9(b), the flapping motions for the two filaments are symmetric with respect to the cylinder, and both swing away from the surface of the cylinder, inducing a pressure recovery upstream of the attaching point. This can be observed in Fig. 10 (lower-right panel), where we plot the vortical contours and pressure distributions for different angles to show how the attachment of a pair of filaments modifies the local fluid flow. It is clearly shown that the vorticity is intensified as the filaments rotate from 0° to 90° (see the left column in Fig. 10), accompanied by the drop of pressure in the wake (see the right column in Fig. 10).

We therefore suggest that the two attached filaments 180° apart meet the requirement of direction adaptive reduction

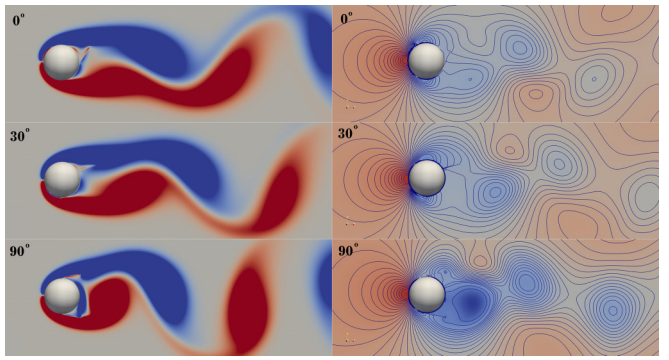

FIG. 10. 256 evenly spaced contours of spanwise vorticity between -100 (blue) and +100 (red) (left column), and their corresponding pressure coefficients between -1.94 and 1.3 (right column). The attachment angles are 0°, 30°, and 90°, respectively, from top to bottom. Note that the vorticity is scaled by ν/D^2, and the pressure coefficient is calculated by $c_p = p/(1/2\rho U_\infty^2)$.

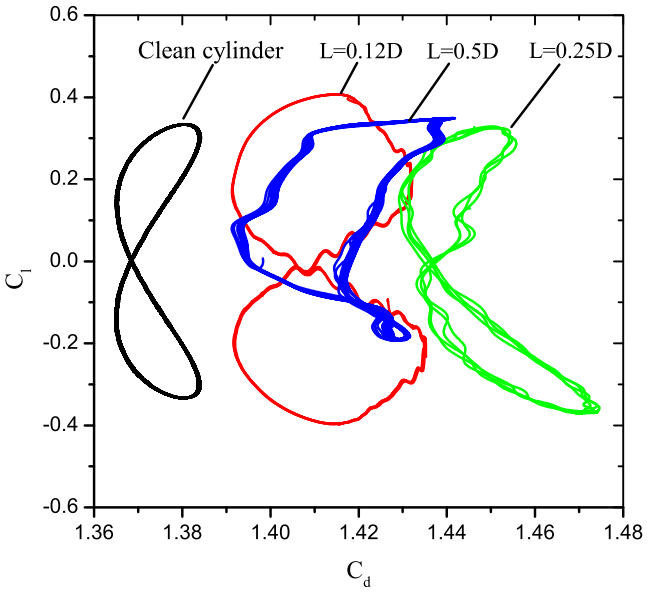

FIG. 11. Phase diagram of the drag and lift coefficients for flow around a circular cylinder with 12 filaments and $\rho_s/\rho_f = 0.1$ and $k_b = 0.005$. Note that the filaments are evenly distributed with one of them attached to the downstream stagnation point, and three lengths are considered.

for average drag forces and lift fluctuations, particularly in the cases of angles smaller than 30°. Within this range, drag reduction and lift fluctuation suppression can be achieved even when the flow reverses. It is worth noting that this drag reduction effect is only effective when the filaments are short enough that the one attached to the front stagnation point can wrap around the cylinder. For long filaments, e.g., with $L = 1.0D$, the filament attached to the upstream surface of the cylinder does not fully attach to the cylinder surface [see Fig. 7(d)], which increases the cross-area of the overall configuration and subsequently the drag force.

C. Attached with multiple filaments

The successful drag reduction by two filaments inspires us to study an even denser distribution of filaments along the cylinder surface (so-called hairy coating [31]), which can be expected to be more adaptive to the change of flow directions for drag reduction. The fluid flow passing a circular cylinder partially coated with hair around the rear surface has been numerically studied [31]. The hair or filaments were modeled as rods. An average drag reduction of 15% and a decrease of lift fluctuations up to 40% associated with the stabilization of the wake were reported by carefully choosing a set of parameters. Here, we adopt a similar approach of hairy coating but by using a more realistic filament model.

We consider the circular cylinder attached with 12 filaments and study three different lengths, $L = 0.12D$, $0.25D$, and $0.5D$. Since the main purpose of our study is to find a drag reduction solution adaptive to the flow directions or insensitive to the variation of incoming flow, we attach the filaments evenly to the cylinder surface, with one attached to the downstream stagnation point. In Fig. 11, we show the phase diagram of the drag and lift coefficients, where

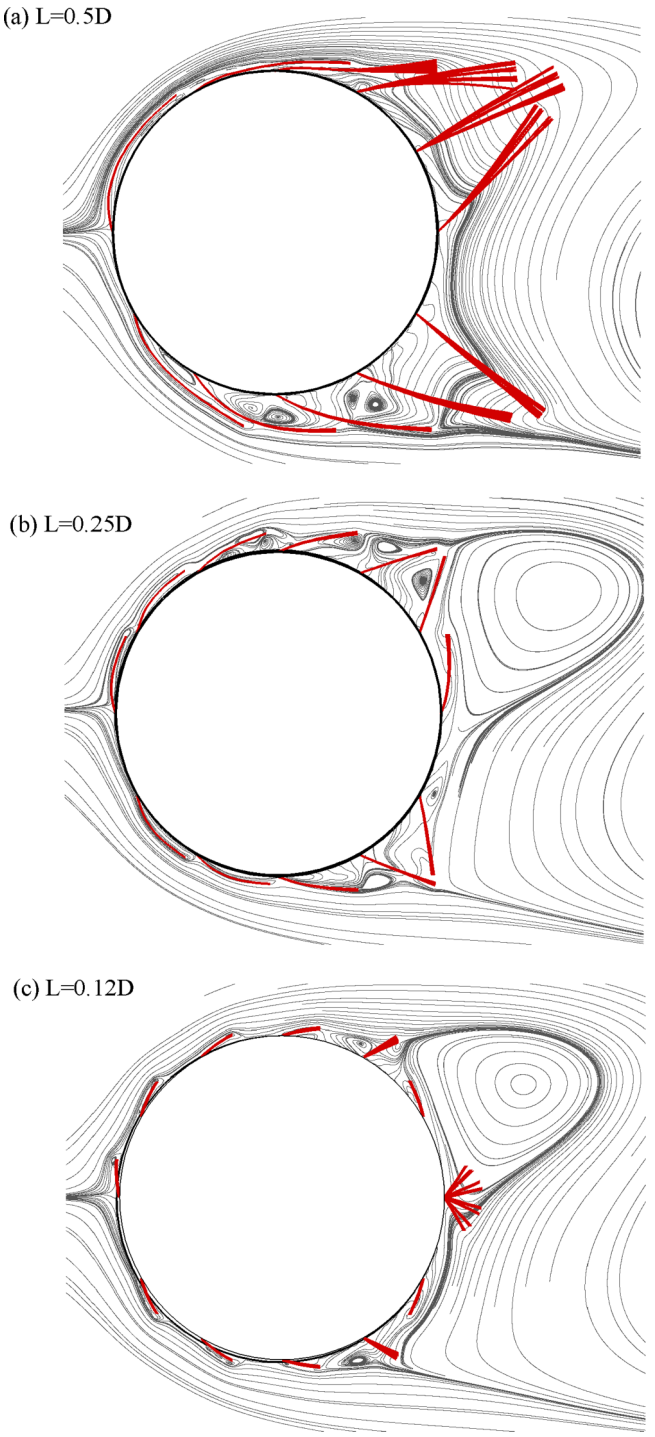

FIG. 12. Ranges of motion for 12 filaments attached to the cylinder, with three different lengths considered, and $\rho_s/\rho_f = 0.1$, $k_b = 0.005$, corresponding to Fig. 11. Instantaneous streamlines have also been included.

we cannot find drag reduction or lift fluctuation suppression. Specifically, we find that the case of $L = 0.12D$ gets a slight increase of drag by 2.8% from the clean cylinder, and the lift fluctuations have not been modified noticeably.

The corresponding ranges of filament motions are shown in Fig. 12, in which we also present the instantaneous streamlines. First, for $L = 0.5D$, the filaments placed at two sides

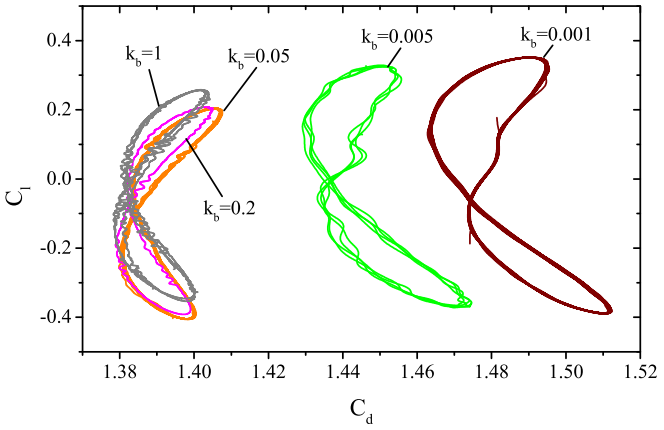

FIG. 13. Phase diagram of the drag and lift coefficients for the flow around a circular cylinder with 12 filaments, with different bendings (k_b), and the length and the density ratio are fixed at $L = 0.25D$ and $\rho_s/\rho_f = 0.1$, respectively

of the wake are pushed apart. The filaments attached to the upper-left surface of the cylinder are stuck to the surface and do not have significant effects on the forces, while those on the lower side of the cylinder relax to their equilibrium positions some distance away from the cylinder surface, increasing the cross-area and creating small vortices in the gaps, as shown in Fig. 12(a). The tips of the leeward side filaments flap at small amplitudes due to the vortex shedding in the wake. We also notice that the vortex shedding occurs at a further downstream location compared to a clean cylinder, similar to the effect by elongating the streamwise length of the cylinder. The small-scale vortices can be also observed for $L = 0.25D$ and $L = 0.12D$ but with smaller scales, as shown in Figs. 12(b) and 12(c). Another interesting behavior we have noticed is that the shortest filament, i.e., $L = 0.12D$, attached at the downstream stagnation point flaps at an extremely large amplitude as seen in Figs. 12(c), due to the alternative vortex shedding in the flow wake. We note that in this case the frequency ratio ω_r takes a small value 0.07 where the filaments are too rigid to be deformed.

It has been implied from Fig. 6 that the drag force and amplitude of lift fluctuation for a single filament can be further reduced by increasing the rigidity, which might also apply to multiple filaments. Here, we show in Fig. 13 the effect of bending rigidity on the 12-filaments case with $L = 0.25D$ and $\rho_s/\rho_f = 0.1$.

We find that both the drag force and lift fluctuation reduce as we increase k_b from 0.001 to 0.05. However, the drag force cannot get further reduction at higher k_b, and in all these cases the drag is higher than that on a clean cylinder.

Moreover, we should point out that the Reynolds number, $\mathrm{Re} = 100$, we have studied here is much lower than that in engineering applications. It is unclear if these configurations of multiple filaments will reduce the drag forces at high Reynolds numbers, where the interactions between turbulent boundary layers and the filaments will be complicated, while in the current low-Reynolds-number study the filaments affect the forces through modulating the vortex shedding in the wake. We believe that there are some fundamental mechanisms in common with those high-Reynolds-number flows in real applications, which needs further investigation.

IV. CONCLUSIONS

We have carried out numerical simulations to study the flow passing a circular cylinder attached with filaments. The immersed boundary method has been implemented into a finite-volume-based numerical solver. Both the circular cylinder and the filaments are modeled as linked Lagrangian points, with their imposed elastic forces, inertial forces, and repulsive forces distributed to the surrounding Eulerian cells by using a discrete Dirac δ function. We have considered different numbers of filaments with various distributions on the surface of the cylinder. The major objective of our study is to examine the impact of various configurations of filaments on the drag and lift forces in a flow with changing directions.

We first consider a single filament attached to the cylinder. By varying the angle of attachment and the properties of the filament, we find a 9.8% drag reduction and a 30.8% lift fluctuation suppression against the clean cylinder when the filament is attached at the downstream stagnation point for length $L = 0.5D$. For two filaments 180° apart and $L = 0.5D$, we observe a drag reduction of 10.8% and the suppression of lift fluctuation by 34.6% as one filament is attached to the downstream stagnation point and the other to the upstream stagnation point. It is important to note that this configuration is direction adaptive and generates desirable control effects when the incoming flow is reversed. The configurations with two filaments 180° apart are also effective at small incident angles, indicating that the control effect of this configuration is insensitive to small variation of incoming flow and is favorable in practical implementations.

Furthermore, we have studied the flow passing a cylinder attached with multiple, or more specifically, 12 filaments, which was called a hairy coating configuration in a previous study [31]. By evenly distributing the filaments, we cannot spot marked drag reduction for the three lengths at a certain set of parameters considered in this study. Nevertheless, this configuration is potentially effective if the flow is turbulent, which requires a further and comprehensive parametric study and is undoubtedly worthy of future investigation.

The main contribution of the current study to the existing drag reduction strategies using rigid or flexible plates or filaments is the direction adaptive control using two filaments 180° apart. This control takes advantage of the flexibility of the filaments. The filament appearing in the wake reduces drag by suppressing vortex shedding, as has been revealed in most of the existing studies on flexible filaments or rigid plates attached to the rear stagnation point of a cylinder [31]. The other filament appearing around the front stagnation point will wrap around the cylinder without adding the cross section of the bluff body, and subsequently the drag of the overall configuration.

ACKNOWLEDGMENTS

This research has been supported by the National Natural Science Foundation of China (Grant No. 11772299) and the Marie Sklodowska-Curie Research and Innovation Staff Exchanges program (Grant No. 777717).

[1] C. Williamson and R. Govardhan, Annu. Rev. Fluid Mech. **36**, 413 (2004).

[2] E. Huse, G. Kleiven, and F. G. Nielsen, Large scale model testing of deep dea risers, *Offshore Technology Conference, 4-7 May, Houston, Texas*, Document ID OTC-8701-MS (Offshore Technology Conference, 1998).

[3] H. Choi, W.-P. Jeon, and J. Kim, Annu. Rev. Fluid Mech. **40**, 113 (2008).

[4] S.-J. Baek and H. J. Sung, Phys. Fluids **10**, 869 (1998).

[5] S. Dennis, P. Nguyen, and S. Kocabiyik, J. Fluid Mech. **407**, 123 (2000).

[6] P. Poncet, J. Fluid Mech. **517**, 27 (2004).

[7] O. Cetiner and D. Rockwell, J. Fluid Mech. **427**, 1 (2001).

[8] J. S. Leontini, D. L. Jacono, and M. C. Thompson, J. Fluid Mech. **730**, 162 (2013).

[9] H. M. Blackburn and R. D. Henderson, J. Fluid Mech. **385**, 255 (1999).

[10] M. K. Chauhan, S. Dutta, B. K. Gandhi, and B. S. More, J. Fluids Eng. **138**, 051105 (2016).

[11] E. Konstantinidis, S. Balabani, and M. Yianneskis, J. Fluid Mech. **543**, 45 (2005).

[12] G. Artana, R. Sosa, E. Moreau, and G. Touchard, Exp. Fluids **35**, 580 (2003).

[13] W.-L. Chen, H. Li, and H. Hu, Exp. Fluids **55**, 1 (2014).

[14] A. Sohankar, M. Khodadadi, and E. Rangraz, Comput. Fluids **109**, 155 (2015).

[15] J. Kim and H. Choi, Phys. Fluids **17**, 033103 (2005).

[16] P. Bearman and J. Harvey, AIAA J. **31**, 1753 (1993).

[17] P. W. Bearman and J. C. OWen, J. Fluids Struct. **12**, 123 (1998).

[18] J. C. Owen, P. W. Bearman, and A. A. Szewczyk, J. Fluids Struct. **15**, 597 (2001).

[19] J. Wang, P. Zhang, S. Lu, and K. Wu, Flow, Turbul. Combust. **76**, 83 (2006).

[20] R. Galvao, E. Lee, D. Farrell, F. Hover, M. Triantafyllou, N. Kitney, and P. Beynet, J. Fluids Struct. **24**, 1216 (2008).

[21] D. W. Allen, D. L. Henning, J. H. Haws, D. W. McMillan, and R. B. McDaniel, US Patent No. 6,561,734.

[22] F. Xie, Y. Yu, Y. Constantinides, M. S. Triantafyllou, and G. E. Karniadakis, J. Fluid Mech. **782**, 300 (2015).

[23] A. Roshko, J. Aeronaut. Sci. **22**, 124 (1955).

[24] K. Kwon and H. Choi, Phys. Fluids **8**, 479 (1996).

[25] S. Mittal, Phys. Fluids **15**, 817 (2003).

[26] B. Stappenbelt, Int. J. Offshore Polar Eng. **20**, 1 (2010).

[27] Y. Jin, L. Yan, H. Qiu, and L. P. Chamorro, Phys. Rev. E **98**, 033106 (2018).

[28] J. Cimbala and K. Chen, Phys. Fluids **6**, 2440 (1994).

[29] S. Shukla, R. Govardhan, and J. Arakeri, J. Fluids Struct. **25**, 713 (2009).

[30] J. Wu, C. Shu, and N. Zhao, Phys. Fluids **26**, 063601 (2014).

[31] J. Favier, A. Dauptain, D. Basso, and A. Bottaro, J. Fluid Mech. **627**, 451 (2009).

[32] M. E. Rosti, A. A. Banaei, L. Brandt, and A. Mazzino, Phys. Rev. Lett. **121**, 044501 (2018).

[33] J. C. Liao, D. N. Beal, G. V. Lauder, and M. S. Triantafyllou, Science **302**, 1566 (2003).

[34] M. Shelley, N. Vandenberghe, and J. Zhang, Phys. Rev. Lett. **94**, 094302 (2005).

[35] H. AitAbderrahmane, M. P. Paidoussis, M. Fayed, and H. D. Ng, Phys. Rev. E **84**, 066604 (2011).

[36] S. Bagheri, A. Mazzino, and A. Bottaro, Phys. Rev. Lett. **109**, 154502 (2012).

[37] J. Lee and D. You, Phys. Fluids **25**, 110811 (2013).

[38] J. Wu, Y. Qiu, C. Shu, and N. Zhao, Phys. Fluids **26**, 103601 (2014).

[39] J. Wu, J. Wu, and J. Zhan, J. Fluids Struct. **66**, 269 (2016).

[40] C. S. Peskin, Ph.D. thesis, Albert Einstein College of Medicine, 1972.

[41] L. Zhu and C. S. Peskin, J. Comput. Phys. **179**, 452 (2002).

[42] F. B. Tian, H. Luo, L. Zhu, J. C. Liao, and X.-Y. Lu, J. Comput. Phys. **230**, 7266 (2011).

[43] W. X. Huang and H. J. Sung, Comput. Methods Appl. Mech. Eng. **198**, 2650 (2009).

[44] W. X. Huang, C. B. Chang, and H. J. Sung, J. Comput. Phys. **230**, 5061 (2011).

[45] Y. Kim and C. S. Peskin, SIAM J. Sci. Comput. **28**, 2294 (2006).

[46] Y. Kim and C. S. Peskin, Comput. Fluids **38**, 1080 (2009).

[47] L. A. Miller and C. S. Peskin, J. Exp. Biol. **212**, 3076 (2009).

[48] Y. Kim, M. C. Lai, and C. S. Peskin, J. Comput. Phys. **229**, 5194 (2010).

[49] W. X. Huang, S. J. Shin, and H. J. Sung, J. Comput. Phys. **226**, 2206 (2007).

[50] D. Goldstein, R. Handler, and L. Sirovich, J. Comput. Phys. **105**, 354 (1993).

[51] H. Jasak, Ph.D. Thesis, Imperial College, University of London, 1996.

[52] F. Xie and J. Deng, Prog. Comput. Fluid Dyn. **18**, 164 (2018).

[53] Y. Kim and C. S. Peskin, Phys. Fluids **19**, 053103 (2007).

[54] S. Xu and Z. J. Wang, J. Comput. Phys. **216**, 454 (2006).

[55] J. Park, K. Kwon, and H. Choi, KSME Int. J. **12**, 1200 (1998).

[56] B. Rajani, A. Kandasamy, and S. Majumdar, Appl. Math. Modell. **33**, 1228 (2009).

[57] P. Bearman, J. Fluid Mech. **21**, 241 (1965).